

# Gas Microchannel Plate–Pixel Detector for X-ray Polarimetry\*

Huan-Bo Feng,<sup>1</sup> Hong-Bang Liu,<sup>1,†</sup> Dong Wang,<sup>2</sup> Zi-Li Li,<sup>3</sup> Shu-Lin Liu,<sup>4,5</sup> Qian Liu,<sup>6</sup>  
Hang-Zhou Li,<sup>7</sup> Bin-Long Wang,<sup>6</sup> Yan-Jun Xie,<sup>1</sup> Zong-Wang Fan,<sup>1</sup> Hui Wang,<sup>2</sup> Ran Chen,<sup>2</sup>  
Di-Fan Yi,<sup>6</sup> Rui-Ting Ma,<sup>6</sup> Fei Xie,<sup>1</sup> Bo Peng,<sup>7</sup> Xiang-Ming Sun,<sup>2</sup> Jin Li,<sup>4</sup> and En-Wei Liang<sup>1</sup>

<sup>1</sup>Guangxi Key Laboratory for Relativistic Astrophysics,

School of Physical Science and Technology, Guangxi University, Nanning 530004, China

<sup>2</sup>PLAC, Key Laboratory of Quark & Lepton Physics (MOE),

Central China Normal University, Wuhan, 430079, China

<sup>3</sup>School of Science, Huzhou University, Huzhou, 313000, China

<sup>4</sup>Institute of High Energy Physics, Chinese Academy of Sciences, Beijing, 100049, China

<sup>5</sup>School of Nuclear Science and Technology, University of Chinese Academy of Sciences, Beijing, 100049, China

<sup>6</sup>School of Physical Science, University of Chinese Academy of Sciences, Beijing, 100049, China

<sup>7</sup>The 13th Research Institute of China Electronics Technology Group Corporation, Shijiazhuang, 050057, China

POLAR-2 is a gamma-ray burst (GRB) polarimeter that is designed to study the polarization in GRB radiation emissions, aiming to improve our knowledge of related mechanisms. POLAR-2 is expected to utilize an on-board polarimeter that is sensitive to soft X-rays (2–10 keV), called low-energy polarization detector (LPD). We have developed a new soft X-ray polarization detector prototype based on gas microchannel plates (GMCPs) and pixel chips (Topmetal). The GMCPs have bulk resistance, which prevents charging-up effects and ensures gain stability during operation. The detector is composed of low-outgassing materials and is gas-sealed using a laser welding technique, ensuring long-term stability. A modulation factor of  $41.28\% \pm 0.64\%$  is obtained for a 4.5 keV polarized X-ray beam. A residual modulation of  $1.96\% \pm 0.58\%$  at 5.9 keV is observed for the entire sensitive area.

Keywords: X-ray polarimetry, Gas Microchannel Plate–Pixel Detector, Gamma-ray Bursts

## I. INTRODUCTION

Gamma-ray bursts (GRBs) are sudden increases in gamma-ray radiation over a short period of time from cosmic space. By measuring the radiation polarization of GRBs, we can gain insight into their outburst mechanisms, as well as the structure and magnetic field configurations of the extreme relativistic jets that produce gamma rays [1]. POLAR is a part of China's Tiangong-2 spacecraft, which was launched on September 15th, 2016. The launch was conducted to measure the GRB polarization in space [2]. During its orbital operation, POLAR detected 55 GRBs and obtained high-precision polarization measurements from 14 of them. According to these novel observations, the evolution of extreme relativistic jets that produce gamma rays may have resulted in rapid changes in the polarization angles, which meant that the observed GRBs were less polarized on average [3]. To answer the scientific questions induced by the POLAR observations and better understand transient radiation mechanisms, radiation region structures, and the surrounding magnetic field configurations, which are long-standing physical problems in GRB research, Chinese and European scientists have jointly proposed an enhanced GRB polarization detection instrument called POLAR-2 [4].

The major scientific objective of POLAR-2 is to obtain high-precision polarization measurements of GRBs from soft X-rays to gamma rays. Among the main components of POLAR-2, the low-energy polarization detector (LPD) measures the polarization of GRBs and their early soft X-ray afterglow. Despite great progress in X-ray astronomy, few soft X-ray polarization observations have been made because of technical measurement limitations. In 1971, the first detection of polarized X-rays from the Crab Nebula was achieved in a rocket sounding experiment [5]. This result was later confirmed by the OSO-8 satellite, which had an on-board polarimeter that accurately measured the polarization at 2.6 keV and 5.2 keV [6]. This nebula's X-ray emission was finally demonstrated to originate from a synchrotron. In 2018, PolarLight, a CubeSat developed by the Tsinghua University team, observed the evolution of the polarization of the Crab pulsar before and after its period glitch [7]. Most recently, the Imaging X-ray Polarimetry Explorer (IXPE), a collaboration between NASA and the Italian Space Agency (ASI), was launched in December 2021 and achieved precise polarization measurements of different kinds of bright X-ray sources during a two-year baseline mission [8]. IXPE is a narrow-field-of-view X-ray polarization detector with grazing-focus optics. It has a large focusing lens barrel, allowing for high detection sensitivity, however its poor maneuverability makes re-pointing and an X-ray transient source survey difficult. IXPE observed polarization in the 2–8 keV X-ray band from the afterglow of GRB221009A for the first time [9]. At a 99% confidence level, IXPE set an upper limit of 13.8% for the polarization degree of the afterglow emission.

The gas pixel detector (GPD) developed by the Istituto Nazionale di Fisica Nucleare (INFN) and Istituto Nazionale di Astrofisica-Istituto di Astrofisica e Planetologia Spaziali

\* This work is supported by Department of Physics and GXU-NAOC Center for Astrophysics and Space Sciences, Guangxi University. This work is supported by the National Natural Science Foundation of China (Grant Nos. 12027803, U1731239, 12133003, 12175241, U1938201, U1732266), the Guangxi Science Foundation (Grant Nos. 2018GXNS-FGA281007, 2018JJA110048).

† Corresponding author, [liubb@gxu.edu.cn](mailto:liubb@gxu.edu.cn)

(INAF-IAPS) in Italy [10, 11] and the time projection chamber (TPC) developed by the Goddard Space Flight Center (GSFC) in the United States [12] demonstrate two more established techniques for detecting X-ray polarization. Both detectors are micropattern gas detectors (MPGDs), where electrons generated by photoelectrons are amplified by a gas electron multiplier (GEM) and then read out by an anode. When the GEM operates, the amplified charge accumulates on the insulating surface in the hole, and this accumulated charge changes the strength of the electric field in the hole, which changes the detector gain.

For a typical GRB event, the energy flux in the 2–10 keV range is approximately  $1 \text{ keV mm}^{-2} \text{ s}^{-1}$  [13]. According to the measurement results obtained by Baldini et al. [14], the gain of the GPD detector is minimally affected by the charging-up effect. For extremely bright GRBs such as GRB221009A, the energy flux reaches  $\sim 100 \text{ keV mm}^{-2} \text{ s}^{-1}$  [15, 16], which can cause a charging-up effect of only a few percent in the GPD detector. Moreover, LPDs are often required to shut down or reduce the detector operating voltage as they pass through the South Atlantic anomaly. It is necessary for the detector's performance to reach a stable state immediately after the operating voltage is applied. This means that the detector must be stable over the short term and its performance should not change significantly with the operating time or counting rate.

This paper presents a new detector structure for X-ray polarization measurements, which was used in an LPD prototype. The detector has a structure similar to that of a GPD. Electron multiplication is obtained by a gas microchannel plate (GMCP), and the read out anode is a pixelated chip, which together comprise the gas microchannel plate-pixel detector (GMPD). The bulk resistance of the GMCP prevent charging-up effects, and the detector has good short-term operational stability. The GMPD itself has lower outgas rates, minimizes working gas pollution, and adopts welding technology for closed gas packaging, which makes it very airtight and increases the detector's life in space. The pitch of the GMCP and size of the pixels in the pixel chip can reach dozens of micrometers, making the detector very sensitive in terms of X-ray polarization measurements. The second section briefly introduces the GMPD's working principle, the third section describes the mechanical structure of the prototype GMPD, the fourth and fifth sections describe the basic properties of the GMPD, the sixth section describes the ability of the GMPD to measure polarized X-rays, and the seventh section summarizes and discusses future perspectives.

## II. GMPD: OPERATING PRINCIPLE

At present, X-ray polarization measurements are mainly performed using three different physical processes: Bragg diffraction, the photoelectric effect, and Compton scattering. The Bragg diffraction method works as a monochromatic polarimetric filter. This means that only a narrow energy band can be observed, which limits the instrument's sensitivity. The derivation of the Klein-Nishina formula for the differ-

ential cross section of Compton scattering shows that a maximum modulation amplitude can be obtained at a polar scattering angle of  $90^\circ$ . However, compared to forward- and back-scattering, the probability of scattering is found to be the smallest at  $90^\circ$ . Compared to Bragg and photoelectric polarimeters, the modulation factor in a Compton polarimeter is generally at a low to medium level [17]. The Compton scattering measurement technique is used to measure high-energy X-rays. To eliminate systematic errors, instruments using Bragg diffraction and Compton scattering must be rotated around the direction of the incident photons [18]. The most efficient process to detect soft X-rays is using the photoelectric effect [19]. When a photon exerts a photoelectric effect on matter, a photoelectron is produced, and the direction of the photoelectron's emission depends on the differential cross-section [20]:

$$\frac{d\sigma^{ph}}{d\Omega} = \frac{\sigma_{ph}^{tot}}{4\pi} \left[ 1 + \frac{b}{2} \left( \frac{3 \sin^2(\theta) \cos^2(\phi)}{(1 + \beta \cos(\theta))^4} - 1 \right) \right], \quad (1)$$

where  $\theta$  and  $\phi$  are the photoelectron polar and azimuthal angles of emission, respectively. The electric vector of the absorbed photon defines the  $\phi = 0$  angular direction. Photoelectrons are emitted with a higher probability parallel to this direction. The orbital asymmetry factor,  $b$ , is equal to 2 for the  $s$  orbital but is less than 2 for the other orbitals. In the first case, the constant term vanishes, and only the  $\cos^2(\phi)$  modulated term remains. The greatest probability of photoelectron emission is parallel to the polarization direction of X-rays, and detectors are used to measure the direction of photoelectron emission and perform statistical analyses on a large number of events to obtain a histogram of the photoelectron emission angle, a modulation curve, and the X-ray polarization information.

GMPD is a micropattern gas detector consisting of a cathode, a GMCP, an anode, and a sealed chamber that can be used to perform meticulous two-dimensional imaging of photoelectrons to achieve X-ray polarization detection. The anode of the detector uses a Topmetal-II pixel chip, which is a silicon pixel detector produced using a  $0.35 \mu\text{m}$  CMOS process. As shown in Fig. 1, the chip consists of a  $72 \times 72$  pixel array and  $6 \times 6 \text{ mm}^2$  effective charge-sensitive region with a pixel spacing of  $83 \mu\text{m}$ . The total area of the chip is  $8 \times 9 \text{ mm}^2$ . The top metal area of a single pixel is  $25 \times 25 \mu\text{m}^2$ , the metal area directly exposed for charge collection is  $15 \times 15 \mu\text{m}^2$ , and the top metal area of each pixel is surrounded by a corresponding guard ring, which can be used to induce a charge in the top metal area. Each pixel electrode is connected to a corresponding charge-sensitive amplifier, which has an equivalent noise charge (ENC) of  $13.9e^-$  at room temperature, with lower noise values at low temperatures such as that produced by exposure to liquid nitrogen. The literature [21, 22] provides more details about the Topmetal-II pixel chip.

As shown in Fig. 2, X-rays travel through the cathode and enter the gas cell, where interaction with atomic electrons produces photoelectrons. These photoelectrons interact within the gas cell ionizing gas atoms, which produces the primary ionization electrons. The primary electrons drift to-

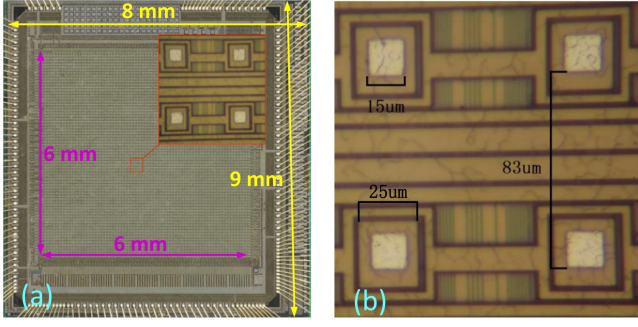


Fig. 1. (Color online) Top view of the Topmetal-II chip, which consists of a  $72 \times 72$  pixel array with a central  $6 \times 6 \text{ mm}^2$  active charge-sensitive area. The total area of the chip is  $8 \times 9 \text{ mm}^2$ . (b) Enlarged view of the pixel matrix, showing the structure of the top metal electrode and guard ring. The pixel spacing is  $83 \mu\text{m}$ , with a top metal area of  $25 \times 25 \mu\text{m}^2$ , where the  $15 \times 15 \mu\text{m}^2$  central region is an exposed electrode formed after the window opening. A passivation layer covers the yellow portion of the photo, which is also utilized for power and ground lines, while the silver metal block represents the electrode after the window opening.

ward the GMCP as a result of an electric field, which provides the necessary gas gain while maintaining the shape of the photoelectron track. Secondary electrons produced by the multiplicative stage drift toward the sensitive area of the pixelated chip as a result of the electric field, where they are collected to induce the read out signal. The signal is then sent to the charge-sensitive preamplifier (CSA) for amplification and conversion into an analog voltage signal, which is then transmitted to the analog output buffer. The analog pulse voltage signal is converted to a digital signal through digital processing and then adjusted by a programmable logic gate array (FPGA) internally. Finally, the data are transmitted to a personal computer (PC) for storage and analysis [23]. The logic circuit of the signal read-out is shown in Fig. 3.

As depicted in Fig. 2, a photoelectron is projected onto the Topmetal-II chip, creating a track. The energy of the photoelectron is equal to the difference between the incident photon energy and binding energy of the gas atom K-shell. The energy of the photoelectrons is gradually lost through collisions with gas atoms. During the collision process, the photoelectrons are subjected to Coulomb scattering by the atomic nucleus, causing them to continuously change direction. In the initial part of the track, the photoelectron has high energy and a low charge density per unit ionization energy. However, toward the end of the track, the photoelectron's energy is rapidly deposited, forming a peak in the distribution of the high charge density known as the Bragg peak. Therefore, the starting end of the track can be identified based on the charge density, and the point of the photoelectric effect can be estimated. The photoelectron's emission direction can be determined based on these features of the track. It is necessary to reconstruct the photoelectron tracks to detect X-ray polarization. The initial emission direction of the photoelectron can be obtained by fitting the first half of its track.

For X-ray polarization measurements, the azimuthal ( $\phi$ )

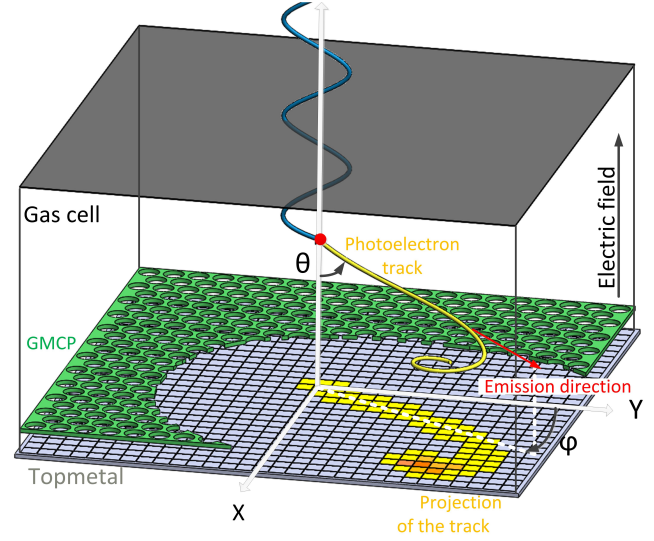


Fig. 2. (Color online) Conceptual design of the GMPD, including the drift plane, GMCP, and readout anode plane (pixel chip). The charge released by the photoelectron is amplified and then collected by readout pixels. Polarization information is derived from the photoelectron tracks imaged by the anode plane.  $\phi$  is the angle between the emission and polarization directions;  $\theta$  is the angle between the photon and photoelectron directions.

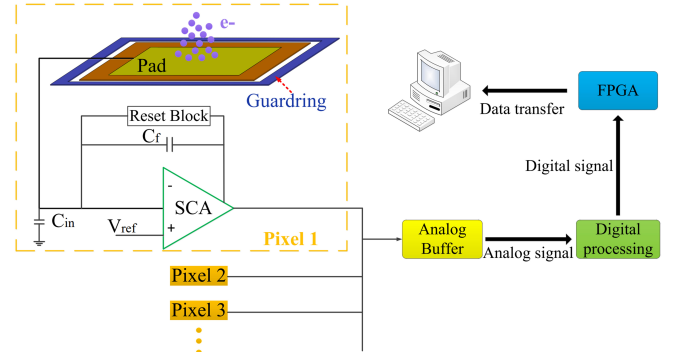


Fig. 3. (Color online) Schematic view of the pixel structure and logic circuit of the signal read-out. In the pixel structure, the central yellow area represents the electrode after the window opening, the brown area represents the electrode covered by the passivation layer, and the outer blue area represents the guard ring. The guard ring is placed around the top metal electrode. This is a ring electrode located in the same topmost metal layer as the top metal electrode but isolated from it. The stray capacitance between the guard ring and top metal electrode is a natural test capacitor. It allows us to apply pulses on the guard ring to inject signals into the CSA and measure its performance.

distribution in the emission direction is obtained by reconstructing and counting a large number of photoelectron tracks. Fig. 4 shows the ideal modulation curves for polarized and unpolarized radiation. In the unpolarized case, the distribution is flat, while in the other case, it peaks near the polarization angle. Based on the photoelectric cross section, the



modulation curve is represented as follows:

$$f(\phi) = A + B \cos^2(\phi - \phi_0). \quad (2)$$

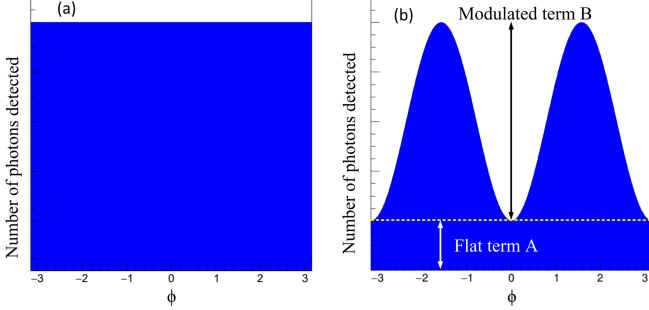


Fig. 4. (Color online) Polarimeter responses: (a) the response of the detector to unpolarized radiation is flat and (b) the response of the detector to polarized radiation is modulated.

A fundamental parameter in polarization measurement is the modulation factor,  $\mu$ , which is the measured modulation amplitude of the detector when exposed to 100% polarized radiation. Modulation factor  $\mu$  is defined as follows:

$$\mu = \frac{M_{max} - M_{min}}{M_{max} + M_{min}} = \frac{B}{2A + B}. \quad (3)$$

In general, the modulation amplitude obtained by a detector when measuring the polarization of radiation with an unknown polarization degree is  $M(P)$ , where  $P$  is the polarization degree of the radiation:

$$P = \frac{M(P)}{\mu}. \quad (4)$$

The performances of different polarimeters can be compared using the minimum detectable polarization (MDP), which is defined as the minimum polarization that can be detected at a confidence level of 99% [24]:

$$MDP = \frac{4.29}{\varepsilon \mu F} \sqrt{\frac{\varepsilon F + b}{TS}}. \quad (5)$$

In this equation  $F$  is the source flux,  $b$  is the background flux,  $\varepsilon$  is the detector efficiency,  $S$  is the collection area, and  $T$  is the observation time. Moreover, without considering the background, the MDP of the polarization detector is found as follows:

$$MDP \propto \frac{1}{\mu \sqrt{\varepsilon}}. \quad (6)$$

Hence, the MDP is inversely proportional to the so-called quality factor,  $Q$ , which is a useful parameter for comparing the sensitivities of different polarization detectors. The quality factor is found as follows:

$$Q = \mu \sqrt{\varepsilon}. \quad (7)$$

### III. DETECTOR STRUCTURE AND ASSEMBLY

The GMPD measures the polarization information of astronomical X-ray sources and has to run for a long time in the space environment. Thus, the GMPD uses a sealed gas design. The plates need to be sealed, which is done using brazing and laser welding, to ensure high gas tightness and good mechanical properties. This ensures that there is no gas leakage in a vacuum environment. Furthermore, the main detector components, including the ceramics, Kova alloys, beryllium, and lead glass, have low outgassing rates, which greatly reduce the pollution of other impurities in the gas. In the space environment, the detector does not need to carry additional replenishment loads and can remain stable for a long time.

The prototype GMPD consisted mainly of a cathode, GMCP, pixel readout chip, metal ceramic tube, and ceramic pedestal, as shown in Fig. 5. To allow more X-rays to enter the detector through the cathode, the X-ray window was composed of 100  $\mu\text{m}$  thick beryllium, which was connected to the Kova alloy frame by brazing to form the cathode of the detector. To fill the detector with working gas, the detector had a gas pipe brazed to the cathode. Through the use of brazing technology, the metal ceramic tube was constructed of three layers of ceramic rings and four layers of Kova alloy rings, with a ceramic ring placed between every two layers of Kova alloy rings. The ceramic layers were used for insulation and positioning between the Kova alloy layers. The Kova alloy rings at both ends of the metal ceramic tube were used to seal the connection with the cathode and pedestal by laser welding. The middle two Kova alloy rings were used to install the exit electrode of the GMCP. The GMCP was installed in the metal ceramic tube, and a support ring was extruded to fix the GMCP. The two electrodes of the GMCP were electrically connected by the Kova alloy to the metal ceramic tube. The ceramic pedestal was also composed of ceramic and Kova alloy. A pixel chip was mounted on the ceramic pedestal and electrically connected to it using gold wire. The information transmission and power supply of the pixel chip were connected to the external environment through 24 pins on the ceramic pedestal.

The manufacturing process of the GMCP involved the use of lead bismuth silicate glass in a process similar to the microchannel plate manufacturing process. The steps included drawing the fiber, stacking multiple fibers, sintering the multifiber array, grinding and polishing, chemically etching the microchannel holes, hydrogen reduction to reduce the bulk resistance, and steam plating metal alloy electrodes with good adhesion and conductivity on the two end faces [24–26]. The structure of the GMCP was similar to that of a thick gas electron multiplier (THGEM) [28], but the insulator in the middle consisted of lead bismuth silicate. The electrodes on both sides were NiCr alloys, and the electrode penetration channel depth was 25–30  $\mu\text{m}$ , as shown in Fig. 6. The diameter of the GMCP was 25 mm, the thickness was approximately 400  $\mu\text{m}$ , the hole diameter was 50  $\mu\text{m}$ , the holes were arranged in a regular triangle, the hole spacing was 60  $\mu\text{m}$ , and the bevel angle of the holes was 0°. The GMCP underwent a hydrogen reduction process for the lead bismuth silicate, with a bulk



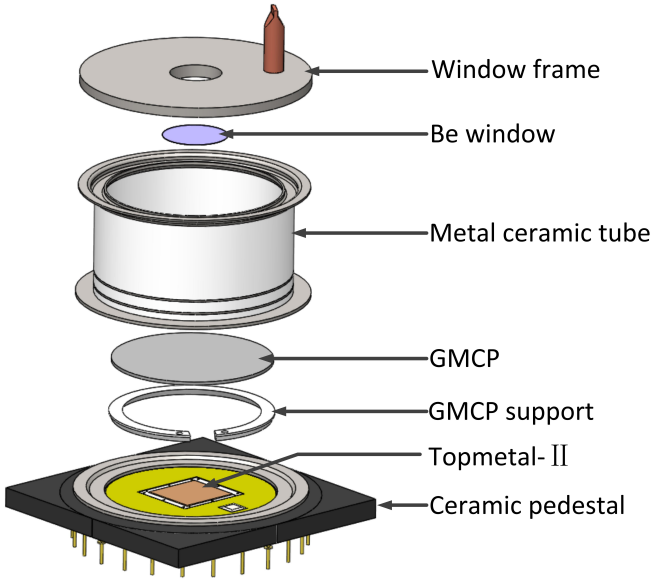


Fig. 5. (Color online) Schematic drawing of the GMPD.

resistance of approximately  $5 \text{ G}\Omega$ , which allowed the release of accumulated charges to eliminate the charging-up effect and improve the short-term gain stability of the GMPD. Compared with a THGEM, the GMCP had a smaller hole spacing, which improved the position resolution of the detector and the ability of the GMPD to detect polarized X-rays. Although the hole spacing of the GEM could reach dozens of micrometers, the outgas rate of its insulator material was higher than that of the GMCP, which was not conducive to long-term working stability.

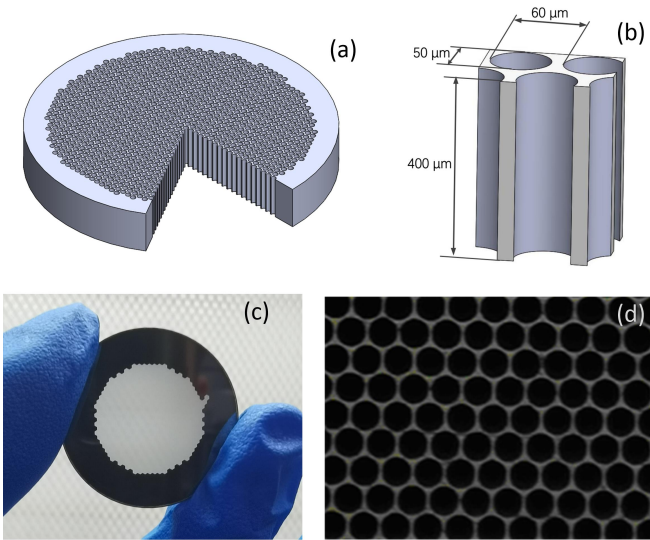


Fig. 6. (Color online) (a), (b) Schematics of the GMCP, (c) picture of the GMCP, and (d) microscopic image of the GMCP.

The encapsulation process of the detector is as follows:

- 1) The GMCP is installed in the metal ceramic tube, and

the stress of the GMCP support ring deformation is used to extrude and fix the GMCP.

- 2) The Topmetal-II chip is fixed to the ceramic base using conductive glue, and gold wire is used to complete the electrical connection between the chip and ceramic pedestal.
- 3) Laser welding technology is used to connect the cathode to the metal ceramic tube.
- 4) Laser welding technology is used to connect the metal ceramic tube to the ceramic pedestal.
- 5) In a vacuum environment, the assembled detector is heated for up to 5 days at a temperature of  $100^\circ\text{C}$ .
- 6) The detector is filled with the working gas, and ultrasonic welding technology is used to seal the copper pipe.

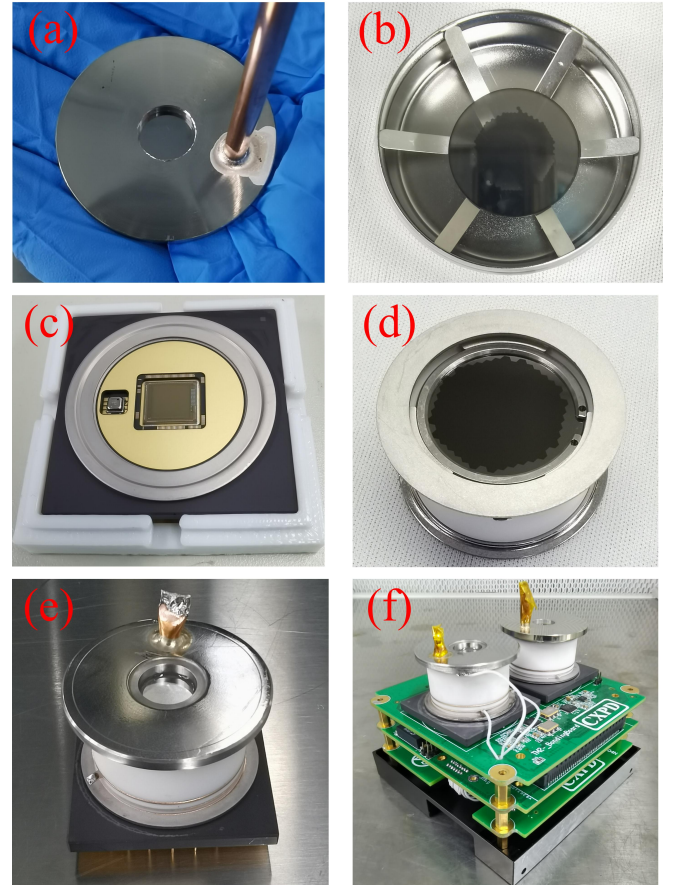


Fig. 7. (Color online) X-ray polarization gas detector assembly photo. (a) Beryllium window and support frame; (b) GMCP; (c) Topmetal-II chip bound to the ceramic pedestal; (d) GMCP mounted in the metal ceramic tube housing; (e) assembled X-ray polarized gas detector; and (f) two gas detectors mounted on a printed circuit board.

The gap between the cathode and GMCP of the detector formed a drift zone with a height of 14 mm; the gap between

the GMCP and anode formed an induction zone with a height of 4 mm. The effective detection area of the detector was  $6 \times 6 \text{ mm}^2$ . The gas tightness of the gas detector was measured using a helium leak detector with a gas leakage rate of  $< 10^{-12} \text{ Pa}\cdot\text{m}^3\cdot\text{s}^{-1}$ .

#### IV. GMPD PERFORMANCE

The working gas of the detector was a mixture of Ne and dimethyl ether (DME). The smaller atomic mass of Ne allowed the photoelectrons to travel longer distances in the gas. These longer tracks could be easily and more accurately reconstructed, resulting in a better polarimetric response. Because diffusion leads to track blur, limiting the ability to reconstruct the direction of photoelectron emission, DME with a low lateral diffusion coefficient was used as a quencher. In general, the angular distribution of Auger electrons is not modulated by X-ray polarization. Thus, the operating energy range was at least twice the K absorption edge limit. A low-Z gas mixture was preferable because the Auger electron energy is larger for higher Z atoms. In the Ne-DME mixture, the energy of the Auger electron was very low compared to the energy of the photoelectron. Therefore, the detector was filled with Ne and DME mixtures with different proportions, using a gas pressure of 1 atm.

To characterize the detector's performance, it was measured using radioactive  $^{55}\text{Fe}$  to produce an X-ray of 5.9 keV. A collimator was placed in front of the detector, and the beam was aligned to illuminate the central area of the detector. Fig. 8 shows the two-dimensional photoelectron track diagram obtained by the GMPD under different gas mixtures, with the X and Y axes showing the coordinates of the image pixels, where the pixel size was the same as that of the actual Topmetal-II chip. The chromaticity of each pixel was proportional to the amount of charge, and the track length was approximately 1 mm. The key to measuring the polarization information of X-rays is obtaining a clear photoelectron track and reconstructing the photoelectron direction and photon absorption point. Using these tracks, it was possible to determine the direction of the photoelectron by judging the characteristics of the Bragg peak at the end of each track, which allowed well-defined separation between the start and end points. A comparison of the tracks under working gases with different proportions made it clear that the tracks became clearer as the DME proportion increased.

Fig. 9 shows the energy spectra of the 5.9 keV X-rays in the operating gas of 50%Ne+50%DME. During the data processing, the noise threshold was  $5\sigma$  in the background, and the energy of each event was the sum of all the pixel values after noise removal. The peaks were fitted using the Gaussian function with an energy resolution of 45.42% (FWHM). Based on these results, it appears that the detector had some difficulty resolving photons at 2 keV compared to those at 6 keV. Our energy resolution was more than double those of energy spectrum measurements by other teams [8]. It was mainly the low readout rate of the Topmetal-II chip and non-uniformity of the pixels that led to spectral degradation. The pixel sig-

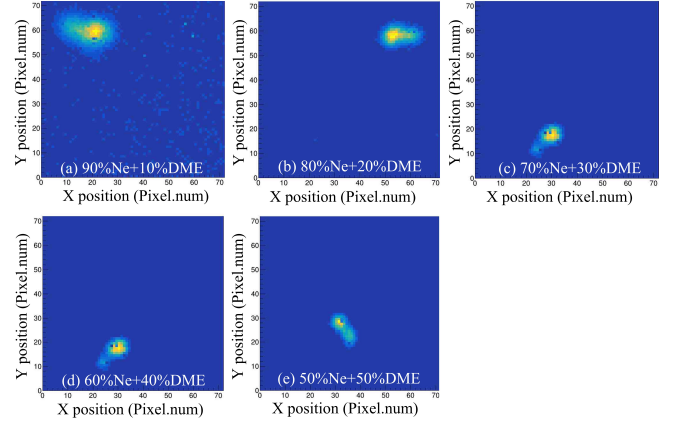


Fig. 8. (Color online) Two-dimensional photoelectron tracks from 5.9 keV X-rays in different gas mixtures. The tracks of (a), (b), (c), (d) and (e) were obtained in 90%Ne+10%DME, 80%Ne+20%DME, 70%Ne+30%DME, 60%Ne+40%DME, and 50%Ne+50%DME, respectively. The dark pixels in the tracks were due to rapid pixel decay, which caused the pixel amplitude value to decay to the baseline level.

nal was read using a row and column sweep method, and the amplitude was the only output when the pixel was scanned, causing an attenuation of the output with respect to the true value. Moreover, the degree of signal attenuation per pixel was inconsistent, with significant differences. In our previous work, we provided a more detailed description of the reasons behind the poor energy resolution of the detector [22]. In addition, some of the multiplied electrons drifted to the anode, while other electrons were collected by the bottom electrode of the GMCP. To overcome the poor energy resolution of the GMPD, we plan to read the signal from the bottom electrode of the GMCP as the energy measurement.

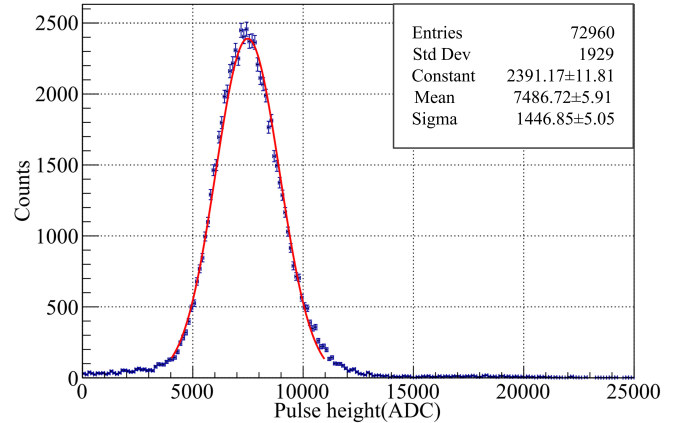


Fig. 9. (Color online) Pulse height distribution measured when the detector is exposed to a 5.9 keV X-ray source, the resulting energy resolution is 45.42% (FWHM). The working gas is 50%Ne+50%DME at 1 atm. The voltage difference of the GMCP is 1260 V, and the drift and induced electric fields are 2 kV/cm and 2.5 kV/cm, respectively. The effective gain is 2100.

A graph of the gain curves of the GMCP in different gas

mixtures is shown in Fig. 10. The maximum effective charge gain corresponded to the occurrence of a discharge. With increasing voltage, the gain of the GMCP increased exponentially. Increasing the DME ratio of the working gas required the application of a higher voltage to the GMCP to obtain the same gain. In addition, the maximum effective gain decreased with an increase in the DME ratio. While increasing the proportion of DME could narrow the photoelectron track, the maximum effective gain that the detector could achieve decreased.

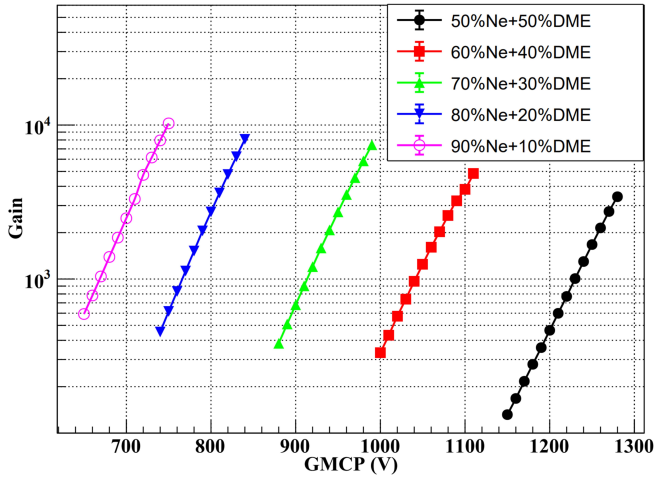


Fig. 10. (Color online) Effective gains as functions of the voltage across the GMCP electrodes for different gas mixtures with various proportions of Ne and DME.

A gas detector's effective charge gain is greatly influenced by the electric field in the drift region. As shown in Fig. 11, the effective gains of the different gases increased rapidly with the drift electric field and then slowly decreased. Because the drift electric field was relatively small, electrons were more likely to be adsorbed by the gas or neutralized by ions. When the drift electric field was large, electrons in the drift area moved downward to obtain higher kinetic energy, and they were more likely to reach the upper surface of the GMCP. Therefore, a suitable drift electric field increased the likelihood of an ionized electron drifting to a GMCP hole, resulting in good detector performance. As the proportion of DME increased, the suitable drift electric field rapidly increased.

A study of the detection efficiency of a GMPD has been carried out with a simulator [29]. The detection efficiency is one of the parameters that determine the sensitivity of a polarimetric detector. When convolved with the transparency of the Be window, this geometric of the GMPD provided an overall peak detection efficiency of more than 25.1% at 2.6 keV, which dropped to approximately 1.28% at 10 keV, as shown in Fig. 12.

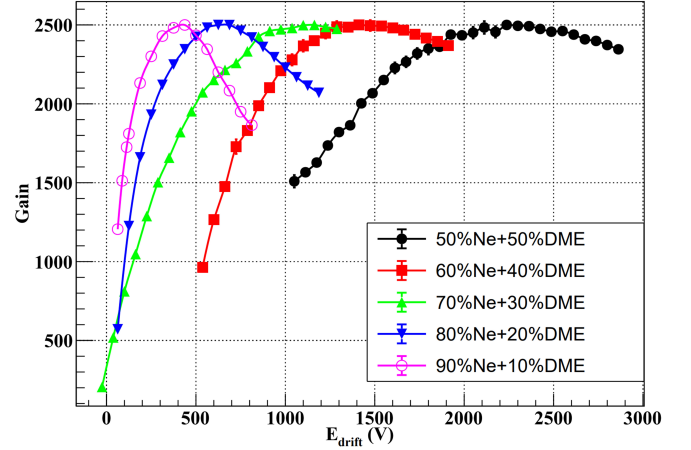


Fig. 11. (Color online) Effective gains as functions of the drifting electric fields for different gas mixtures with various proportions of Ne and DME.

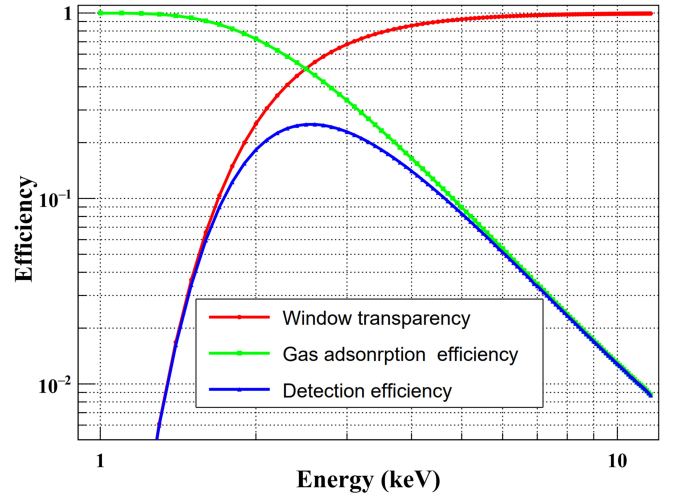


Fig. 12. (Color online) Detection efficiency as a function of energy. The calculation assumed 14 mm of 50%Ne+50%DME at 1 atm, and a Be window of 100  $\mu\text{m}$ .

## V. GMPD OPERATING STABILITY

The LPD measures GRBs, where the X-ray intensity of a GRB suddenly increases for a short period of time and then rapidly decreases. Therefore, the response of the detector to the counting rate was investigated while considering the charging-up effect of the GMCP on the detector. In this experiment, an X-ray tube was used as a particle source, and its current was adjusted to produce X-rays with different intensities. A collimator was placed directly above the detector to control the divergence angle of the photons. The collimator had a depth of 2 cm and diameter of 3 mm. In the beginning, the X-ray intensity level was relatively high, and the detector counting rate reached 140 counts/s/mm<sup>2</sup>. The detector gain remained stable after approximately 8 h of measurements, as shown in Fig. 13. The GMCP gain remained stable when



the counting rate was reduced from 140 counts/s/mm<sup>2</sup> to 60 counts/s/mm<sup>2</sup>. The GMCP gain remained stable for several subsequent reductions of the detector counting rate. The final detector counting rate increased from 2.0 counts/s/mm<sup>2</sup> to 130 counts/s/mm<sup>2</sup>, and the GMCP gain did not change significantly. Based on the measurement results, the gain of the detector remained constant in different counting rate environments. This was because of the GMCP's inherent bulk resistance, which eliminated charging-up effects. The LPD's insensitivity to the counting rate makes it suitable for measuring transient sources such as GRBs.

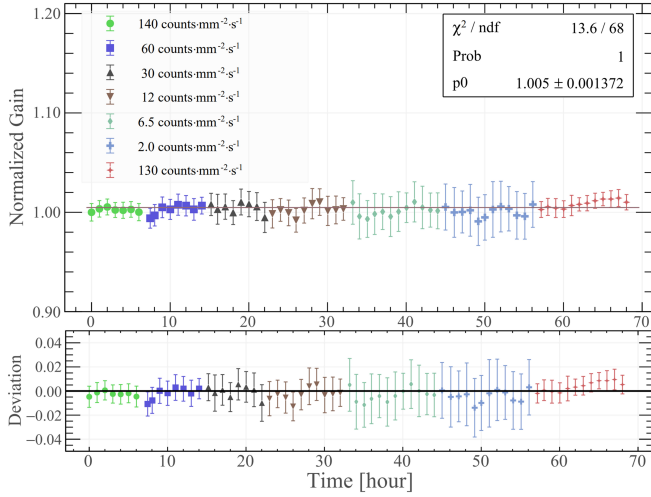


Fig. 13. (Color online) Curve of the detector gain with the counting rate. The working gas is 50%Ne+50%DME at 1 atm.

When operating in future space orbits, the LPD will require frequent switching on and off, or changes to the operating voltage, making it necessary to monitor the gain of the detector over time. Immediately before measurement, the operating voltage of the detector is turned off, and the detector is left to stand for more than 24 h to clear the accumulated charge, stabilizing and initializing the system. As shown in Fig. 14, the gain of the detector did not change significantly over 5 h, and the gain stability was better than 5%. This was because of the bulk resistance of the GMCP, which prevented charge accumulation on the insulation layer surface and maintained a constant multiplied electric field. As a result, the detector was free from charging-up effects and exhibited good short-term operational stability.

To investigate the long-term stability of the GMPD, we filled the detector with a 90%Ne+10%DME mixture at a gas pressure of 1.1 atm. The detector's gain and energy resolution were monitored over the course of more than a year, and there was no evidence that they were deteriorating. When the detector was not in use, it was stored in a laboratory environment. This method excluded serious gas leaks and gas mixture contamination. The gain gradually increased, and the energy resolution slowly decreased during the first 150 days after filling it with the working gas, but after 150 days, it became more stable. In our initial assessment, we assumed that the small changes in the previous period could have been a

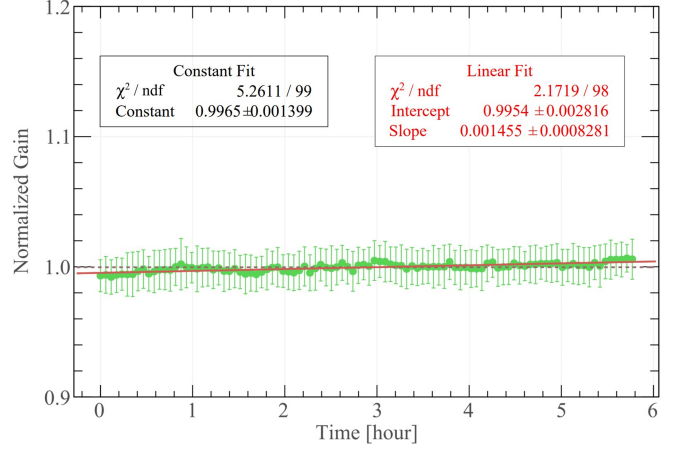


Fig. 14. (Color online) Relative gain of the detector over time after an initial increase in the operating voltage. The working gas is 50%Ne+50%DME at 1 atm.

result of a trace material exchange between the detector material and mixed gas after the detector was filled with the working gas, resulting in a stable state within 150 days of the detector being filled with the working gas. In addition, the stability of the detector lasted for longer periods of time depending on the curve change trend. Fig. 15 displays a distinct behavior in comparison to Fig. 13, because the gain in the initial measurements showed an increase, which could be attributed to the utilization of a different gas mixture. In this context, it is necessary to consider the long-term trends of the gain and energy resolution. Conducting further tests on the gain behavior using various additional gas mixtures will aid in identifying the cause of this phenomenon.

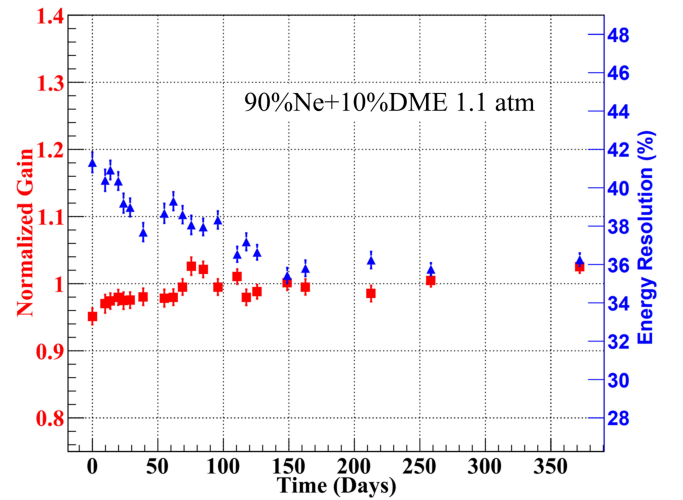


Fig. 15. (Color online) Long-term monitoring results for the detector's normalized gain (Red) and energy resolution (Blue). The working gas was 90%Ne+10%DME at 1.1 atm. The voltage difference of the GMCP was 700 V, and the drift electric field and induced electric field were 0.5 kV/cm and 2.5 kV/cm, respectively.

As the LPD performs sky patrol observations following the

Chinese Space Station (CSS), it is exposed to both direct solar irradiation and no solar irradiation, leading to changes in the probe temperature. Hence, we conducted a study on the detector gain's response to temperature by subjecting the detector to different temperature environments and measuring its gain. Referring to Fig. 16, it can be observed that the detector gain remained relatively stable within the temperature range of 20–40 °C. This was because the detector chamber was sealed, and the working gas density in the chamber remained constant at different temperatures. Therefore, the number of molecules per unit volume of gas did not change, and the gain of the detector remained stable despite changes in temperature. The temperature control requirement for future detectors operating in orbit could be estimated to be  $30\text{ °C} \pm 10\text{ °C}$ .

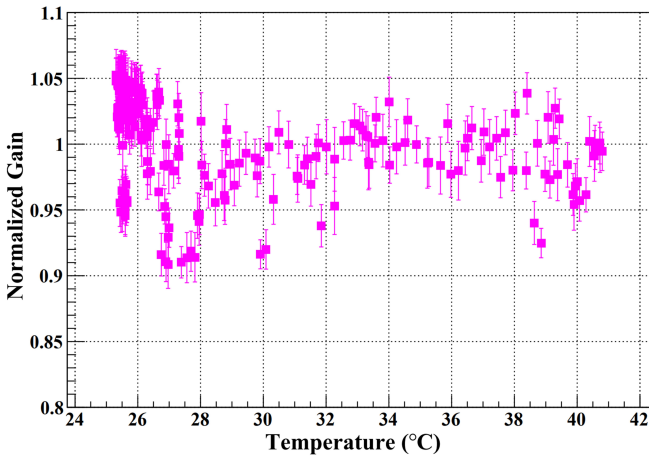


Fig. 16. (Color online) Response curve of the detector gain to temperature. The working gas was 50%Ne+50%DME at 1 atm.

## VI. POLARIMETRY

The working gas when measuring the X-ray polarization of the GMPD was 50%Ne+50%DME, with a gas pressure of 1 atm. To reduce the transverse diffusion coefficient of the working gas, a gas mixture containing a large proportion of DME was chosen. However, as the proportion of DME increased, the highest effective charge gain of the detector decreased, the signal-to-noise ratio decreased, and the photoelectron tracks became blurry, which adversely affected the sensitivity of the GMPD during polarized X-ray detection. Additionally, as the proportion of DME increased, the negative high voltage requirements of the detector increased, and if there was a discharge, it was easier to damage the detector device, increasing the safety risks. The working gas for IXPE's GPD detectors is pure DME, and they have an energy resolution of  $\sim 17\%$  (FWHM) when measuring 5.9 keV X-rays [14]. The energy resolution of GMPD detectors is approximately twice that of GPD detectors. Hence, this poor energy resolution was not due to gas mixture, but was mainly caused by the need for improved Topmetal-II pixel chips.

To characterize the detector's ability to measure polarized X-rays, based on the equipment described by Muleri et al. [30], we constructed a fully polarized X-ray source in the laboratory, which mainly consisted of X-ray tubes and crystals that could generate fully polarized monochromatic X-rays by Bragg diffraction. The anode material of the X-ray tube was titanium, and the crystal material was LiF (100). This X-ray source generated polarized X-rays with an energy of 4.5 keV, and based on the energy of the X-rays and information from reference [30], the polarization degree of the diffracted X-rays could be derived to be 99.19%. The spectrum of crystal diffraction was acquired using an Amptek XR-100 SDD X-ray detector, with an energy resolution of 153 eV FWHM at 5.9 keV. The diffraction angle was estimated based on the energy of the diffracted X-rays. A Ruishikeni RS130A CCD imager with  $1280 \times 1024$  5- $\mu\text{m}$  pixels was used to image the polarized beam. As shown in Fig. 17, X-rays that satisfied the Bragg diffraction condition exhibited a Bragg arc on the imager. Such an X-ray source produced a polarized X-ray of 4.5 keV. To produce the unpolarized X-ray source, radioactive  $^{55}\text{Fe}$  was used to produce an X-ray with an energy of 5.9 keV.

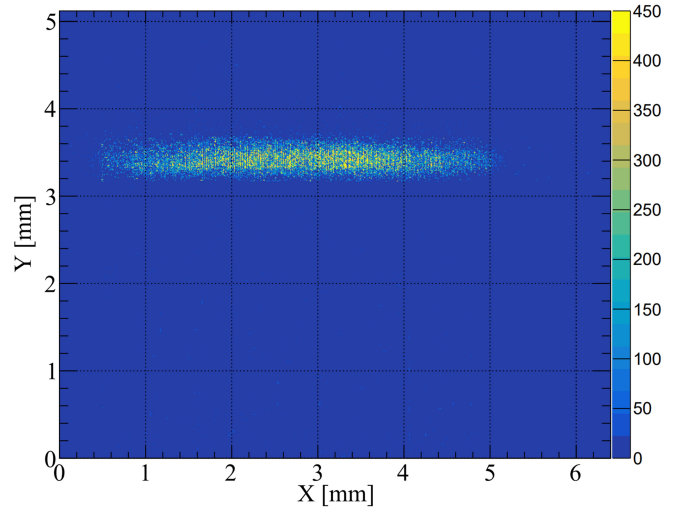


Fig. 17. (Color online) Image obtained with the CCD imager of the photons generated with the polarized source.

To determine the polarization information of an X-ray, we needed to screen and reconstruct the photoelectron tracks obtained. Three factors were considered when screening these tracks: 1) tracks that hit a total of less than 25 pixels were removed because the photoelectrons were emitted almost perpendicular to the detector plane; the initial part of the track was easily confused with other parts, making the reconstruction of the photoelectron emission angle difficult. 2) The tracks where only partial information was retained were also discarded because they were not precisely reconstructed. There were two reasons for removing these tracks. The first was that the Topmetal-II chip utilizes a row scan readout method, and some pixels will have already been scanned and read when the track signal reaches their surface. The second was the projection of photoelectrons onto the edge of the

Topmetal-II chip. 3) An event with two or more independent charge clusters was also discarded. These events were likely to occur when multiple photoelectron tracks arrived simultaneously at the Topmetal-II chip. As a result, approximately 40% of the events were discarded from the analysis. Track reconstruction was carried out to determine the direction of photoelectron emission and the point of photon absorption, as illustrated in Appendix 1.

The histogram of the photoelectron emission angle measured with 4.5 keV polarized X-rays is shown in Fig. 18. The modulation curve was obtained by fitting Eq. (2), and the modulation factor was calculated to be 41.28% with a statistical error of  $\pm 0.64\%$  using Eq. (3). The modulation factor is the response of the detector to the degree of modulation of the fully polarized X-ray. It is one of the most significant parameters of a polarized X-ray detector and directly affects the detector's observation sensitivity to the polarized X-ray source. Based on the measurement results of the GMPD for polarized X-rays at 4.5 keV, with a detection efficiency of 10.75%, and considering an event residual rate of 60% for track reconstruction, the quality factor of the GMPD for 4.5 keV X-rays was calculated to be 10.48% using formula Eq. (7). Bellazzini et al. reported a quality factor of  $\sim 11\%$  for a GPD with a working gas of 50%Ne + 50%DME at 1 atm [31]. Based on the quality factor of the polarimetric detectors, the sensitivity difference between the GPD and GMPD detectors was small. Note that the quality factor was not the same as that for the IXPE, because it was based on an older detector and different mixture. The polarization source image was obtained using the reconstructed absorption points (Fig. 19). The source image on the GMPD was compatible with the image observed on the CCD, but the GMPD image of the spot was larger than that observed on the CCD. This could be attributed to the low accuracy of the reconstruction algorithm.

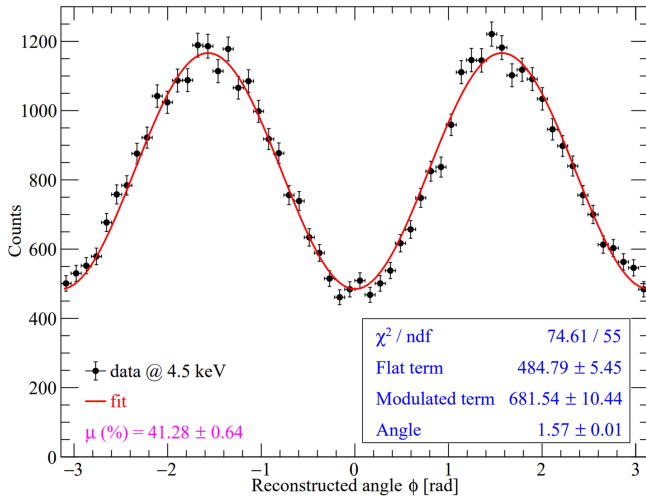


Fig. 18. (Color online) Modulation curve obtained from 4.5 keV polarized X-ray measurements in a 50%Ne+50%DME mixture.

Fig. 20 shows the measured modulation curve of 5.9 keV unpolarized X-rays, where the residual modulation factor was 1.96% with a statistical error of  $\pm 0.58\%$ . This could be used

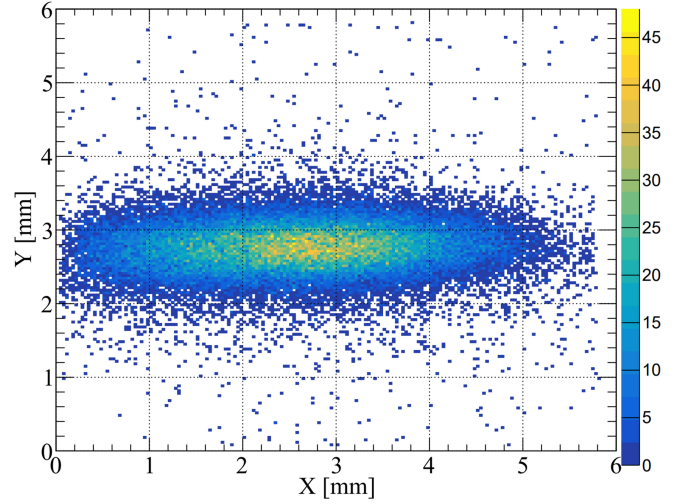


Fig. 19. (Color online) Image of the polarized source on the GMPD with a 50%Ne+50%DME mixture.

to estimate the residual modulation of the detector due to systematic effect. This result was beyond the statistical error limits, with the existence of the modulation. Compared to the results reported in [14], the systematic effect of this detector was relatively large. Factors that could have led to this result include the non-uniform gain of the GMCP, the non-uniformity of the pixels in the Topmetal-II chip, and the non-uniformity of other structures in the detector. In the future, we plan to conduct a thorough investigation of the origins of this systematic effect and implement necessary corrections and calibrations.

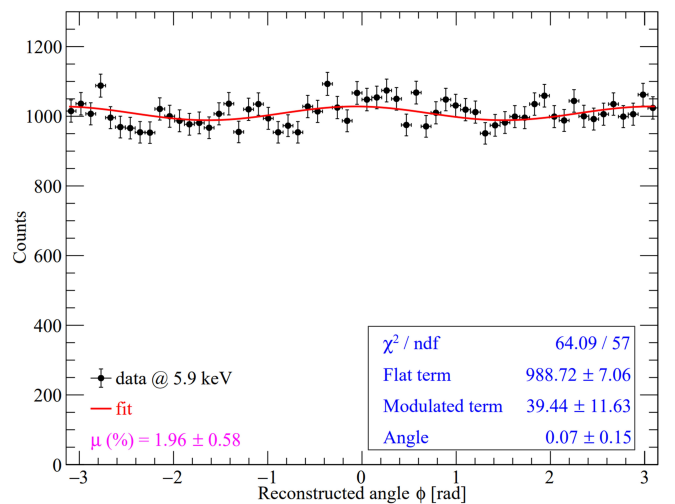


Fig. 20. (Color online) Modulation curve obtained from 5.9 keV unpolarized X-ray measurements in a 50%Ne+50%DME mixture.



## VII. SUMMARY AND OUTLOOK

We presented the structure and performance test results of a GMPD in this paper. The GMPD was the prototype for the PLD of POLAR-2, which is to be launched from the CSS. The GMPD used the GMCP as a gas electron multiplier and the Topmetal-II pixel chip as a readout anode to collect multiplied electrons. The GMCP was a detector gas electron multiplier device, and its short-term stability was better than 5% because of its several-G $\Omega$  bulk resistance and elimination of the charging-up effect. The detector gain remained stable with different operating time periods and counting rates. Therefore, the detector would be ideal for observing transient sources where the flux of particles changes rapidly. At the same time, this would allow the detector to enter a stable working state after the initial application of the operating voltage.

As a sealed gas detector, advanced welding techniques were used to completely encapsulate the GMPD. This resulted in excellent airtightness and a small leakage rate, which was  $< 10^{-12}$  Pa·m<sup>3</sup>·s<sup>-1</sup>. The materials used for the GMPD had low-outgassing rates, and the state of the working gas could remain stable for a long time, with good long-term working stability. After injecting a gas mixture of 90%Ne+10%DME (at 1.1 atm) into the detector, no significant performance changes were observed over the next 370 days. The detector could still operate stably for long periods of time in the space environment without carrying additional rechargeable gas loads. Moreover, the detector gain remained relatively stable within a temperature range of 20–40 °C.

Measuring the performance of the detector using X-rays produced a precise two-dimensional track of the photoelectrons, enabling a clear differentiation between the interaction point, emission direction, and Bragg peak of the track. This is essential for X-ray polarization measurement. We tested the detector's effective gain, energy spectrum, energy resolution, and other basic properties, and its basic performance response was similar to those of other MPGDs. The detector operated with a maximum effective gain of 3000 in a 50%Ne+50%DME working gas and an energy resolution of 45.42% for X-rays with an energy of 5.9 keV. We obtained X-ray polarization information with a modulation factor of  $41.28\% \pm 0.64\%$  for polarized X-rays of 4.5 keV and a residual modulation factor of  $1.96\% \pm 0.58\%$  for unpolarized X-rays of 5.9 keV. The feasibility of using the GMPD for polarized X-ray detection was verified.

Because the GMCP + Topmetal structure was first used in gas polarization detectors, it does not have an optimal performance because the detector structure, Topmetal-II chip, working gas, and photoelectron track reconstruction algorithm have not been systematically optimized. Therefore, the GMPD performance is poorer than those of GPD detectors reported in the literature [14]. In the near future, we will primarily reduce the size of the pixels on the Topmetal-II chip, which is comparable to the hole spacing on the GMCP. In addition, improvements in the readout method of the Topmetal-II chip and a reduction in interpixel inhomogeneities are expected to improve the energy resolution and position resolution of the

gas detector, as well as its ability to detect polarized X-rays. It is particularly important to optimize the structure and working gases of the detector using polarization X-rays of different energies, which will further improve the detector's sensitivity.

## VIII. APPENDIX 1: EVENT RECONSTRUCTION PROCESS

(1) First, the barycenter of the track is calculated using the coordinates  $(x_i, y_i)$  and charge values,  $p_i$ , (as the weight) of each pixel in the track. The formula for calculating the coordinates of the barycenter of the track is as follows:

$$x_c = \frac{\sum_{i=1}^n x_i p_i}{\sum_{i=1}^n p_i}, \quad (8)$$

$$y_c = \frac{\sum_{i=1}^n y_i p_i}{\sum_{i=1}^n p_i}, \quad (9)$$

where  $n$  represents the number of pixels in the track. In Fig. 21, the position of the red pentagon labeled “barycenter” represents the barycenter of the track.

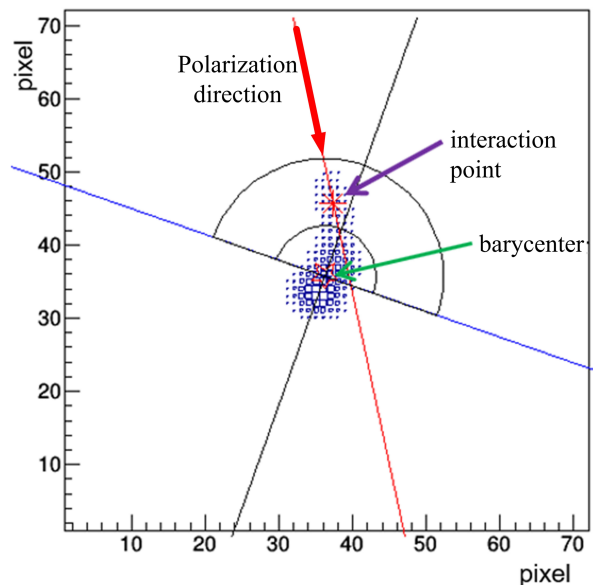


Fig. 21. (Color online) Schematic diagram of photoelectron track reconstruction.

(2) The track direction is determined based on the second moment. Centering the track in  $(x_c, y_c)$ , the second moment of the charge distribution is calculated as follows:

$$M_2(\psi) = \frac{\sum_{i=1}^n p_i [(x_i - x_c) \cos(\psi) + (y_i - y_c) \sin(\psi)]^2}{\sum_{i=1}^n p_i}, \quad (10)$$

where  $\psi$  is the angle between the track direction and X-axis. This is used to determine the axis of the charge distribution of the minimal or maximal extension. When  $dM/d\psi = 0$ ,

the angle that maximizes or minimizes  $M_2$  is obtained [32]. The maximum and minimum angles ( $\psi_{max}$  and  $\psi_{min}$ , respectively) are separated by  $90^\circ$ , and they determine the longitudinal and transverse second moment (represented by the black and blue lines in Fig. 21, respectively). At this point,  $\psi_{max}$  defines the angle between the track direction and X-axis.

(3) Because of the accumulation of Bragg peaks at the tail of the track, the calculation of the third moment can separate the head and tail of the track, determining the half-zone where the photoelectron interaction point is located. The third moment is calculated for  $\psi_{max}$  as follows:

$$M_3(\psi_{max}) = \frac{\sum_{i=1}^n p_i [(x_i - x_c) \cos(\psi_{max}) + (y_i - y_c) \sin(\psi_{max})]^3}{\sum_{i=1}^n p_i} \quad (11)$$

The distance between each pixel and the  $(x_c, y_c)$  coordinates is estimated in  $M_2$  units. Pixels that have a distance sign different from that of  $M_3(\psi_{max})$  are removed, which are within the region where the photoelectron Bragg peak is located.

Next, we calculate the distance,  $l_i$ , from the barycenter to

the pixel point  $(x_i, y_i)$  within the head zone of the track.

$$l_i = \sqrt{(x_i - x_c)^2 + (y_i - y_c)^2} \quad (12)$$

Then, we find the maximum value,  $l_{max}$ , among the  $l_i$  values. Draw two semicircles with the barycenter as the center in the head zone of the track, with radii of  $R_1$  and  $R_2$ . The formulas to calculate  $R_1$  and  $R_2$  are as follows:

$$R_1 = 1.2l_{max}, \quad (13)$$

$$R_2 = ql_{max}, \quad (14)$$

where  $q \in [0, 1]$  is a variable that can be adjusted, and the actual parameters used were obtained after several rounds of empirical testing. The pixels in the annular region are preserved as the head of the track.

(4) The charges of the pixels are then used to estimate  $M_2$  for the remaining head of the track. The new barycenter is marked in Fig. 21 as the “interaction point,” which is the position of the asterisk, and it is the algorithm’s estimate of the interaction point. The new track direction is illustrated in red in the diagram, while the arrow indicates the emission direction of the photoelectron 2D projection obtained via the algorithm [33].

- 
- [1] K. Toma, T. Sakamoto, B. Zhang et al., Statistical properties of gamma-ray burst polarization. *Astrophys J.* **698**, 1042 (2009). <https://dx.doi.org/10.1088/0004-637X/698/2/1042>
  - [2] N. Produit, T.W. Bao, T. Batsch et al., Design and construction of the POLAR detector. *Nucl Instrum Meth A.* **877**, 259–268 (2018). <https://doi.org/10.1016/j.nima.2017.09.053>
  - [3] S.N. Zhang, M. Kole, T.W. Bao et al., Detailed polarization measurements of the prompt emission of five gamma-ray bursts. *Nat Astron.* **3**, 258–264 (2019). <https://doi.org/10.1038/s41550-018-0664-0>
  - [4] N. De Angelis, J.M. Burgess, F. Cadoux et al., Development and science perspectives of the POLAR-2 instrument: a large scale GRB polarimeter. *arXiv preprint arXiv:2109.02978* (2021). <https://doi.org/10.48550/arXiv.2109.02978>
  - [5] R. Novick, M.C. Weisskopf, R. Berthelsdorf et al., Detection of X-ray polarization of the Crab nebula. *Astrophys J.* **174**, L1 (1972). <https://doi.org/10.1086/180938>
  - [6] M.C. Weisskopf, E.H. Silver, H.L. Kestenbaum et al., A precision measurement of the X-ray polarization of the Crab Nebula without pulsar contamination. *Astrophys J.* **220**, L117–L121 (1978). <https://doi.org/10.1086/182648>
  - [7] H. Feng, H. Li, X. Long et al., Re-detection and a possible time variation of soft X-ray polarization from the Crab. *Nat Astron.* **4**, 511–516 (2020). <https://doi.org/10.1038/s41550-020-1088-1>
  - [8] M.C. Weisskopf, P. Soffitta, L. Baldini et al., Imaging x-ray polarimetry explorer: prelaunch. *J Astron Telesc Instrum Syst.* **8**, 026002 (2022). <https://doi.org/10.1117/1.JATIS.8.2.026002>
  - [9] M. Negro, N. Di Lalla, N. Omodei et al., The IXPE view of GRB 221009A. *Astrophys J Lett.* **946**, L21 (2023). <https://doi.org/10.3847/2041-8213/acba17>
  - [10] R. Bellazzini, G. Spandre, M. Minuti et al., A sealed Gas Pixel Detector for X-ray astronomy. *Nucl Instrum Meth A.* **579**, 853–858 (2007). <https://doi.org/10.1016/j.nima.2007.05.304>
  - [11] F. Muleri, P. Soffitta, L. Baldini et al., Performance of the Gas Pixel Detector: an x-ray imaging polarimeter for upcoming missions of astrophysics. *Proc Spie.* **9905**, 1401–1407 (2016). <https://doi.org/10.1117/12.2233206>
  - [12] J.K. Black, R.G. Baker, P. Deines-Jones et al., X-ray polarimetry with a micropattern TPC. *Nucl Instrum Meth A.* **581**, 755–760 (2007). <https://doi.org/10.1016/j.nima.2007.08.144>
  - [13] P.A. Evans, A.P. Beardmore, K.L. Page et al., Methods and results of an automatic analysis of a complete sample of Swift-XRT observations of GRBs. *Mon Not R Astron Soc.* **397**, 1177–1201 (2009). <https://doi.org/10.1111/j.1365-2966.2009.14913.x>
  - [14] L. Baldini, M. Barbanera, R. Bellazzini et al., Design, construction, and test of the Gas Pixel Detectors for the IXPE mission. *Astropart Phys.* **133**, 102628 (2021). <https://doi.org/10.1016/j.astropartphys.2021.102628>
  - [15] Z.H. An, S. Antier, X.Z. Bi et al., Insight-HXMT and GECAM-C observations of the brightest-of-all-time GRB 221009A. *arXiv preprint arXiv:2303.01203* (2023). <https://doi.org/10.48550/arXiv.2303.01203>
  - [16] M.A. Williams, J.A. Kennea, S. Dichiara et al., GRB 221009A: Discovery of an Exceptionally Rare Nearby and Energetic Gamma-Ray Burst. *Astrophys J Lett.* **946**, L24 (2023).

- <https://doi.org/10.3847/2041-8213/acbcd1>
- [17] T. Chattopadhyay, Hard X-ray polarimetry—an overview of the method, science drivers, and recent findings. *J Astrophys Astron.* **42**, 106 (2021).  
<https://doi.org/10.1007/s12036-021-09769-5>
- [18] S. Fabiani, Instrumentation and future missions in the upcoming era of X-ray polarimetry. *Galaxies.* **6**, 54 (2018).  
<https://doi.org/10.3390/galaxies6020054>
- [19] E. Costa, P. Soffitta, R. Bellazzini et al., An efficient photoelectric X-ray polarimeter for the study of black holes and neutron stars. *Nature.* **411**, 662–665 (2001).  
<https://doi.org/10.1038/35079508>
- [20] P.K. Ghosh, *Introduction to Photoelectron Spectroscopy*. John Wiley and Sons: Hoboken, NJ, USA, (1983).
- [21] M. An, C. Chen, C. Gao et al., A low-noise CMOS pixel direct charge sensor, Topmetal-II<sup>+</sup>. *Nucl Instrum Meth A.* **810**, 144–150 (2016).  
<https://doi.org/10.1016/j.nima.2015.11.153>
- [22] Z. Li, H. Feng, X. Huang et al., Preliminary test of topmetal-II<sup>+</sup> sensor for X-ray polarization measurements. *Nucl Instrum Meth A.* **1008**, 165430 (2021).  
<https://doi.org/10.1016/j.nima.2021.165430>
- [23] H. Wang, D. Wang, R. Chen et al., Electronics system for the cosmic X-ray polarization detector. *Nucl Sci Tech.* **34**, 64 (2023).  
<https://doi.org/10.1007/s41365-023-01221-3>
- [24] R. Bellazzini, F. Angelini, L. Baldini et al., X-ray polarimetry with a micro pattern gas detector with pixel readout. *Ieee T Nucl Sci.* **49**, 1216–1220 (2002).  
<http://dx.doi.org/10.1109/TNS.2002.1039640>
- [25] T. Gys, Micro-channel plates and vacuum detectors. *Nucl Instrum Meth A.* **787**, 254–260 (2015).  
<https://doi.org/10.1016/j.nima.2014.12.044>
- [26] W. Cao, B. Zhu, X. Bai et al., High-sensitivity and long-life microchannel plate processed by atomic layer deposition. *Nanoscale Res Lett.* **14**, 1–8 (2019).  
<https://doi.org/10.1186/s11671-019-2983-1>
- [27] H.Z. Cai, Q.Y. Luo, K.X. Lin et al., Development of an ultra-fast detector and demonstration of its oscillographic application. *Nucl Sci Tech.* **33**, 72 (2022).  
<https://doi.org/10.1007/s41365-022-01055-5>
- [28] H.B. Liu, Y.H. Zheng, Y.G. Xie et al., Study of the THGEM detector with a reflective CsI photocathode. *Chinese Phys C.* **35**, 363 (2011).  
<https://dx.doi.org/10.1088/1674-1137/35/4/008>
- [29] X.F. Huang, H.B. Liu, J. Zhang et al., Simulation and photoelectron track reconstruction of soft X-ray polarimeter. *Nucl Sci Tech.* **32**, 67 (2021).  
<https://doi.org/10.1007/s41365-021-00903-0>
- [30] F. Muleri, P. Soffitta, L. Baldini et al., Low energy polarization sensitivity of the Gas Pixel Detector. *Nucl Instrum Meth A.* **584**, 149–159 (2008).  
<https://doi.org/10.1016/j.nima.2007.09.046>
- [31] R. Bellazzini, F. Angelini, L. Baldini et al., Gas pixel detectors for X-ray polarimetry applications. *Nucl Instrum Meth A.* **560**, 425–434 (2006).  
<https://doi.org/10.1016/j.nima.2006.01.046>
- [32] A. Di Marco, E. Costa, F. Muleri et al., A weighted analysis to improve the x-ray polarization sensitivity of the imaging x-ray polarimetry explorer. *Astrophys J.* **163**, 170 (2022).  
<https://doi.org/10.3847/1538-3881/ac51c9>
- [33] R. Bellazzini, A. Brez, E. Costa et al., Photoelectric X-ray polarimetry with gas pixel detectors. *Nucl Instrum Meth A.* **720**, 173–177 (2013).  
<https://doi.org/10.1016/j.nima.2012.12.006>